

# Investigation of the Evolution of the Oxide Scale Formed on 310 Stainless Steel Oxidized at 600 °C in Oxygen with 40% Water Vapour Using FIB and TEM

F. Liu · J. E. Tang · H. Asteman · J.-E. Svensson ·  
L.-G. Johansson · M. Halvarsson

Received: 3 March 2008 / Revised: 5 November 2008 / Published online: 3 December 2008  
© Springer Science+Business Media, LLC 2008

**Abstract** Detailed microstructure investigations were performed on oxide scales formed on 310 stainless steel exposed isothermally at 600 °C to O<sub>2</sub> with 40% water vapour for 1–336 h. FIB microscopy was used to study the evolution of the surface morphology and to prepare cross-section TEM thin foils of the oxide scales. The foils were investigated by analytical transmission electron microscopy. The results showed that a thin protective base oxide scale had formed after 1 h. Due to Cr loss from the oxide scale through water vapour induced Cr evaporation, local breakaway oxidation occurs, resulting in the formation of oxide nodules. The development of these nodules depends on whether a new Cr-rich healing layer is formed or not. A model for the evolution of the oxide scale is proposed based on the results regarding the composition and distribution of various phases in the oxide scale and subjacent steel.

---

F. Liu (✉) · J. E. Tang · M. Halvarsson  
Microscopy and Microanalysis, Department of Applied Physics, Chalmers University  
of Technology, 412 96 Göteborg, Sweden  
e-mail: fang.liu@fy.chalmers.se

H. Asteman · J.-E. Svensson  
Environmental Inorganic Chemistry, Department of Chemical and Biological Engineering,  
Chalmers University of Technology, 412 96 Göteborg, Sweden

*Present Address:*

H. Asteman  
Schmidt + Clemens GmbH + Co. KG, Central Technology Development,  
P.O. Box 1140, 51779 Lindlar, Germany

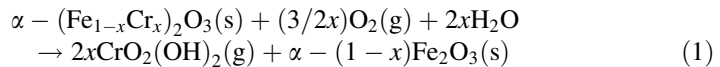
L.-G. Johansson  
Department of Chemical and Biological Engineering, High Temperature Corrosion Centre,  
Chalmers University of Technology, 412 96 Göteborg, Sweden

**Keywords** Fe–Cr–Ni alloy · High temperature oxidation · Water vapour · Microstructure · FIB · TEM · EDX

## Introduction

Stainless steels have good oxidation resistance at elevated temperatures, owing to the formation of a thin layer of slow-growing, continuous, dense and adherent Cr-rich  $\alpha$ -(Cr,Fe)<sub>2</sub>O<sub>3</sub>. These steels are often used in applications where high temperature oxidation is a major concern. The operating environment of these materials often contains both oxygen and water vapour.

Water vapour has long been identified as a critical factor in stainless steel high temperature oxidation [1–6]. Different explanations for the role of water vapour have been proposed [2, 7–11]. Some earlier work suggested that the material transport through the oxide scale is altered in the presence of water vapour. Increased mass transport of oxygen [7], iron [8] and chromium [9] has been reported. Some authors believe that water vapour may cause the chromium rich scale to decompose via a series of self-catalyzed reactions [10]. Asteman et al. [12] reported a mass loss for 304L (wt%: 18.5 Cr, 10.2 Ni, 1.4 Mn) stainless steel samples and a Cr depletion in the oxide scales after prolonged exposures at 600 °C in the presence of oxygen and water vapour. It was proposed that the phenomena resulted from water vapour induced Cr evaporation from the oxide scale, probably in the form of CrO<sub>2</sub>(OH)<sub>2</sub>(g):



Cr evaporation causes Cr depletion in the oxide scale. Increasing gas flow rate, water vapour and oxygen concentrations and temperature speed up the evaporation process. A continuous and rapid Cr supply from the steel to the oxide is essential for maintaining a good oxidation resistance. If the Cr concentration in the oxide scale drops below a critical level, due to chromia evaporation and insufficient Cr supply from the steel, the protective Cr-rich oxide will transform into a non-protective Fe-rich oxide, and breakaway oxidation occurs [12, 13]. Cr evaporation and related phenomena were also reported for the lower alloyed ferritic FeCr steel X20 (wt%: 11.0 Cr, 0.65 Ni, 0.45 Mn) [14, 15], and for the higher alloyed austenitic steels 310 (wt%: 24.9 Cr, 19.2 Ni, 1.55 Mn) and 353MA (wt%: 26.0 Cr, 32.6 Ni, 1.42 Mn) [16, 17]. Results supporting the water vapour induced Cr evaporation mechanism have also been provided by other authors [18, 19].

Detailed information on the microstructure of the steel and the oxide scale is essential for understanding the oxidation behavior. Surface morphologies for oxide scales have long been observed using electron microscopy [20]. However, with respect to cross-section views of the oxide scale, most previous work was done using metallographic cross-section preparation methods, which often damage the oxide scales, since they tend to be brittle. Furthermore, in spite of the practical interest for e.g. thermal power plant applications, very little work has been done on the oxide scales of commercial stainless steels, especially at intermediate

temperatures (around 600 °C) in well-controlled atmospheres and for short exposure times.

Previously, we have investigated the effect of water vapour on the oxidation behavior of the 310 austenitic stainless steel at 600 °C by comparing the microstructure of the oxide scales and steel substrates from samples exposed in dry oxygen, O<sub>2</sub> containing 40% H<sub>2</sub>O at a low flow rate (0.5 cm/s) and O<sub>2</sub> containing 40% H<sub>2</sub>O at a high flow rate (5 cm/s) [21]. The results clearly show that the oxidation rate increases in the presence of water vapour. In dry O<sub>2</sub>, a thin protective Cr-rich (Cr,Fe)<sub>2</sub>O<sub>3</sub> was formed. In O<sub>2</sub> with 40% H<sub>2</sub>O at the low flow rate, the oxide remained thin, but with indications of Cr loss by CrO<sub>2</sub>(OH)<sub>2</sub> evaporation. In O<sub>2</sub> with 40% H<sub>2</sub>O at the high flow rate local breakaway in the form of large oxide nodules was observed.

Our previous papers on this subject primarily describe the situation before and after the break-down of the protective oxide. In contrast, the present paper is a time-resolved study, showing the different stages in the process of break-down of the protective oxide which is induced by chromium depletion. This work investigates the detailed microstructure of the oxide scales formed on 310 stainless steel oxidized isothermally at 600 °C in O<sub>2</sub> + 40% H<sub>2</sub>O with 5 cm/s gas velocity with exposure times between 1 and 336 h. Focused ion beam (FIB) microscopy was used to investigate the morphology of the oxide scales and to prepare site-specific cross-sections and TEM membranes. A combination of transmission electron microscopy (TEM) and energy dispersive X-ray spectroscopy (EDX) was used to obtain structural and chemical information. Our aim is to elucidate the evolution of the oxide scale as a function of time and to understand the oxidation mechanisms for type 310 stainless steel in oxygen and water vapour containing atmospheres at 600 °C.

## Experimental

### Exposure

The chemical composition of the 310 stainless steel used in this work is given in Table 1. 15 mm × 15 mm × 2 mm steel coupons were ground with SiC paper to 1000 mesh and polished with 1 μm diamond spray and then cleaned in acetone and ethanol using ultrasonic agitation. Three such polished coupons were set into three parallel slits on an alumina plate. Then the alumina plate, together with the three coupons, was placed into a horizontal furnace. The furnace is fitted with a 48 mm diameter SiO<sub>2</sub>-glass tube. Within the tube each coupon had one of its 15 mm × 2 mm sides facing the flow rate. This set-up minimizes the disturbance

**Table 1** Nominal composition of the 310 stainless steel alloy used in this work

Element	Cr	Ni	Mn	Si	Mo	Fe
Wt.%	24.9	19.2	1.55	0.45	0.34	Balance

caused by the presence of multiple samples in the furnace. All the exposures were carried out isothermally, and the temperature was kept at  $600 \pm 3$  °C. The reaction gas consisted of 60 vol.% O<sub>2</sub> and 40 vol.% H<sub>2</sub>O. The gas flow velocity was always 5 cm/s. The exposure times were 1, 24, 72, 168 and 336 h.

### Focused Ion Beam Microscopy

An FEI 200 THP FIB system equipped with “xp” milling software was used in this work. The system can be used both for imaging and subsequent well-controlled local milling. Features of interest can thus be investigated not only in plan view but also in cross-section view after careful *in situ* milling. Thin (100 nm) cross-section foils for TEM analysis were also prepared in the FIB system.

The system has a liquid gallium ion source. The normal working accelerating voltage is 30 kV. Different ion beam currents from 1 picoampere (pA) to 20,000 pA can be chosen. Usually 10 pA is used for imaging to minimize the ion-induced damage to samples, while still getting enough signal to noise ratio in the images. Secondary electrons induced by the ion beam are detected for imaging. The spatial resolution for imaging is about 5 nm for the system. Beam currents in the sequence: 20,000, 3,000, 1,000, 500 and 100 pA were used for coarse milling, fine milling and final polishing in order to mill away the material rapidly and to obtain a relatively re-deposition free cross-section surface after the final milling step.

The following procedures were used for preparing self-supported TEM samples. (i) A 400 μm thick strip was cut from the steel coupon using a low speed saw. (ii) The strip was ground to around 150 μm thickness by wet mechanical polishing using 240 and then 800 grid SiC-paper. (iii) Half disks with 3 mm diameter were stamped. (iv) The disks were polished to 50 μm in thickness using 15 and 6 μm diamond suspension in sequence. (v) A 1.5 μm (width) × 20 μm (length) × 2 μm (height) platinum (Pt) strip was deposited onto the feature, which was chosen to be investigated further using TEM. The Pt deposition was done in the FIB by using an attached gas injection system. (vi) In the FIB, by using the typical beam current sequence mentioned above, 10 μm (depth) × 20 μm (width) × 100 nm (thickness) electron transparent TEM windows could be produced.

### Analytical Transmission Electron Microscopy

A Philips CM 200 FEG transmission electron microscope, which has a field-emission gun as the electron source, was used in this work. It was operated with an accelerating voltage of 200 kV. A Link Isis EDX (Energy Dispersive X-ray analysis) system is attached to the microscope. The software of the Link Isis system can be used to produce STEM (Scanning Transmission Electron Microscopy) images, EDX maps, EDX spot analyses and EDX linescans. The electron transparent windows produced in the FIB were analyzed by a combination of these techniques. Due to the technical difficulty of quantifying the light anion elements (i.e. O), the linescans presented in this article show element concentrations as a percentage of the total cation content, i.e. all cations present add up to 100 wt.%.

## Results

### Overview of Oxide Scale Morphology

The low magnification plan-view images in Fig. 1 show the surfaces of samples exposed for different times. All the oxide scales feature networks of lines. The lines are the less oxidized steel grain boundary regions (see also Figs. 2, 3), and are present already after 1 h. They are most clearly visible on the surface of the 24-h sample and appear vaguer after longer exposures.

Except for the 1-h sample, all the sample surfaces exhibit oxide nodules on some of the steel grains. Most nodules are rounded in shape and distributed randomly (Fig. 1c, e). In some cases large elongated nodules are observed, with a preferential

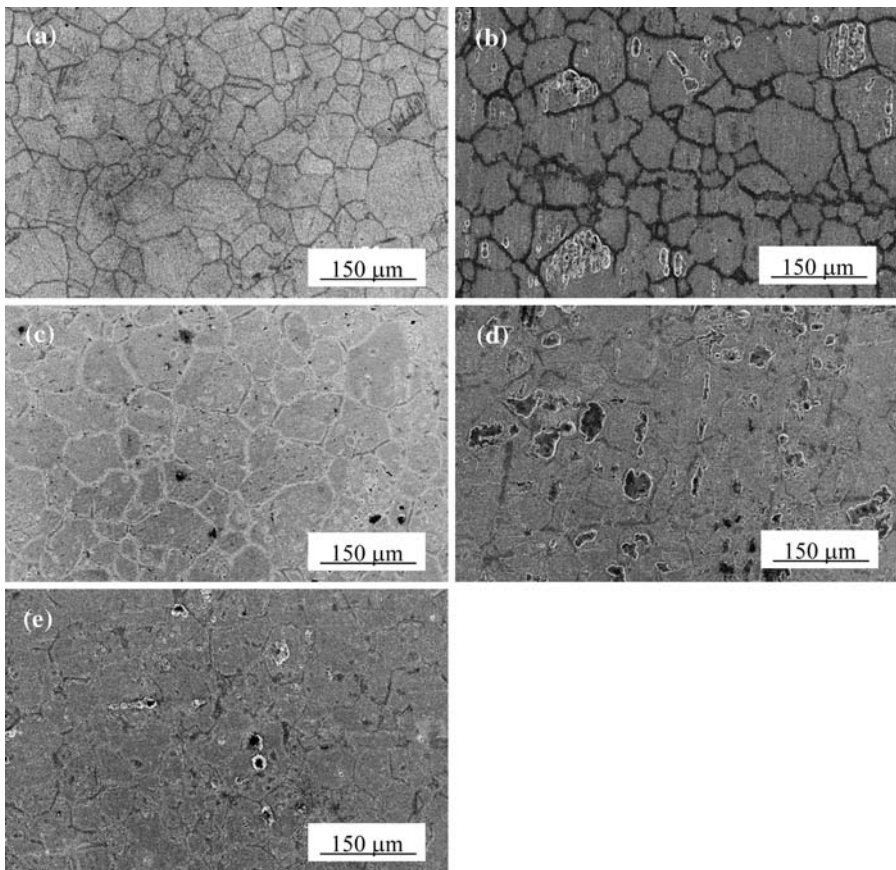


**Fig. 1** Low magnification plan-view FIB images of samples oxidized for different durations **a** 1 h, **b** 24 h, **c** 72 h, **d** 168 h and **e** 336 h. All the sample surfaces exhibit a network of lines reflecting the underlying steel grain boundaries. In addition to the thin base oxide scale, which covers most of the surface, thicker oxide nodules exist on all the samples except the 1-h sample

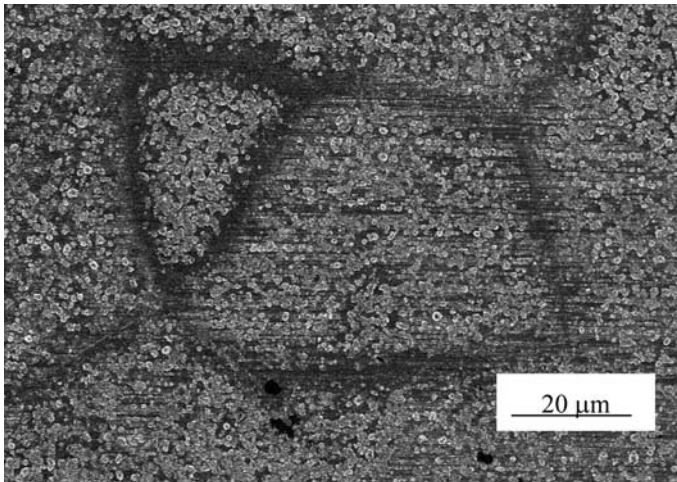


**Fig. 2** FIB image of the 1-h sample, showing the base oxide consisting of submicron oxide particles. The steel grain boundary regions are less oxidized

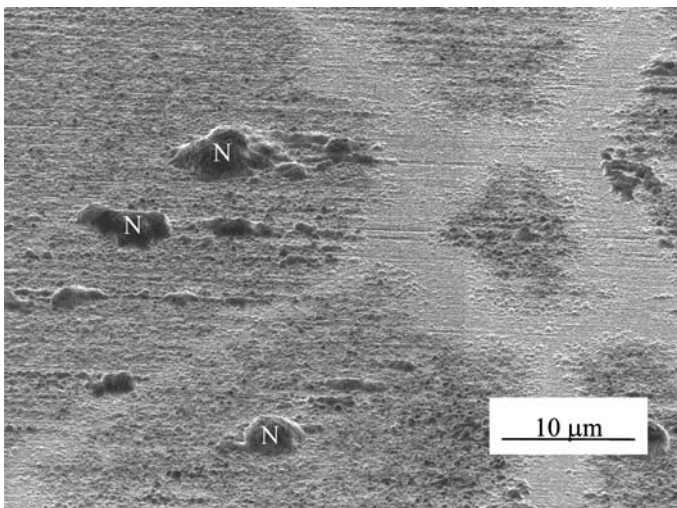


**Fig. 3** FIB image of the 24-h sample (tilted 45°). The width of the protective steel grain boundary regions varies. Some large oxide nodules (N) have formed on some of the steel grains

orientation (Fig. 1b, d). It is believed that the specific direction of alignment of the nodules follows the polishing direction.

#### Evolution of the Oxide Features

The detailed surface morphology of the 1-h sample is shown in Fig. 2. There are a large number of fine oxide particles on top of the steel grains. These particles have

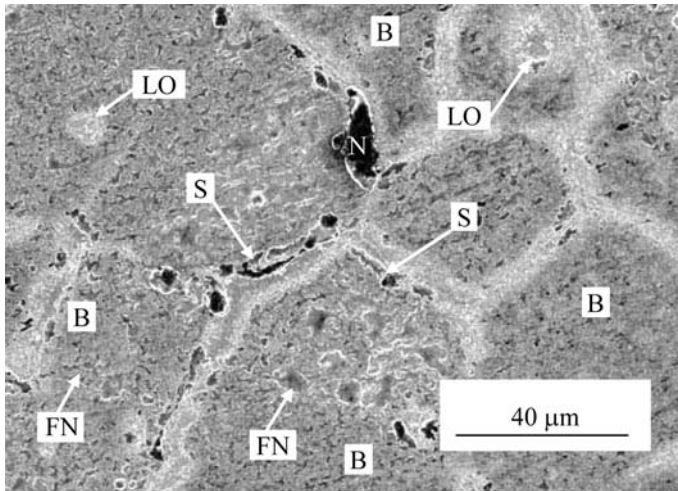


**Fig. 4** FIB image of the 72-h sample. In addition to the base oxide (B), and large oxide nodules (N) (see also Figs. 8a and 13 below), less oxidized patches (LO), thin flat oxide nodules (FN) and “snowbanks” (S) have formed

sizes ranging from a few hundred nanometers to approximately one micrometer. In the steel grain boundary regions, the oxide scale is smooth and thin. In fact, the oxide scale on the entire sample is rather thin and is referred to as the *base oxide* in this article.

After 24 h most of the surface is still covered by a thin base oxide. The smooth morphology of the steel grain boundary regions is shown very clearly in Fig. 3. The widths of these regions vary, ranging from about 1 to 5 μm on this sample. This variation in width was found for all exposure times. In addition to the base oxide and steel grain boundary regions, the oxide nodules (labeled “N”) have now formed.

After 72 h exposure, additional oxide features were observed (see Fig. 4), flat irregular-shaped oxide nodules (labeled “FN”) with a length of 1–5 μm appearing in large numbers. Some of these flat nodules growing along the steel grain boundaries resemble banks of snow along a street, and are thus referred to as “snowbanks” (labeled “S”). In addition to the steel grain boundary regions, there are other well-protected areas on some steel grains. They are rounded with a typical diameter of a few micrometers. They are referred to as less-oxidized patches (labeled “LO”).

The oxidized surfaces of the 168 and 336-h samples (Figs. 5, 6) exhibit the same features as the 72-h sample. However, the oxide nodules, including the flat ones, have merged and grown much larger compared to those on the 72-h sample. Furthermore, many of the large oxide nodules on the 336-h sample are covered by blade-like oxide features (Fig. 6), which can be up to 5 μm in length. Based on analysis by EDX, showing the blade-like features to consist mainly of iron oxide, they are considered to be made up of hematite. The different features were analyzed in more detail with the FIB and the TEM and the results are presented in section “Detailed Microstructure of the Oxide”.

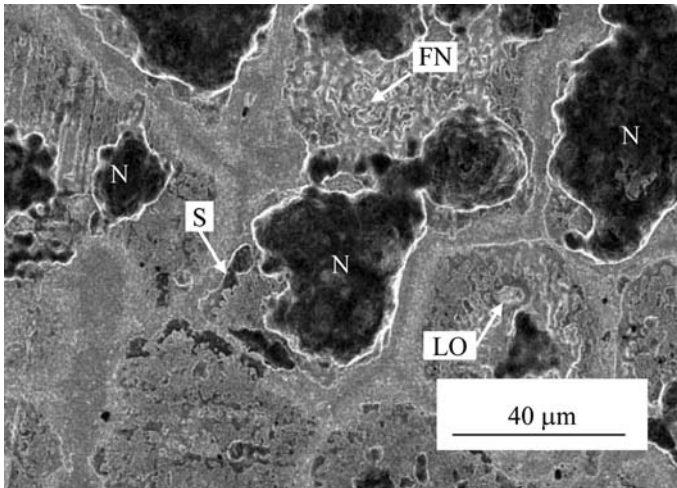


**Fig. 5** FIB image of the 168-h sample. All the oxide features formed on the 72-h sample exist also after 168 h. However, the number and size of the large oxide nodules have increased

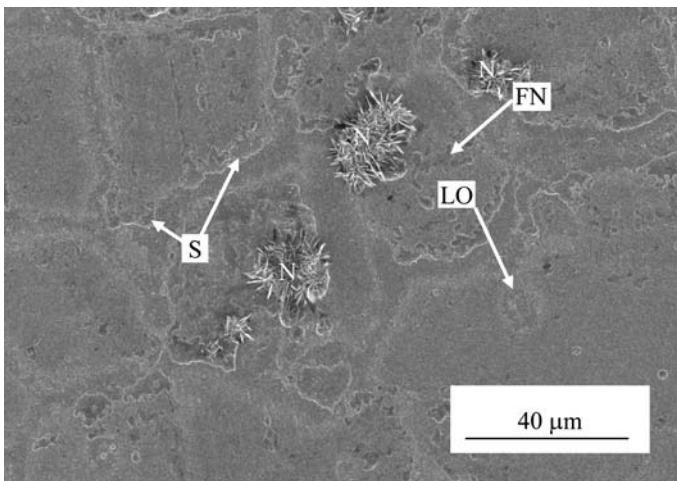


**Fig. 6** FIB image of the 336-h sample. The oxide features are similar to those on the 72- and 168-h samples. However, many of the large oxide nodules are now covered by oxide blades

#### Detailed Microstructure of the Oxide

Oxide scales were milled in the FIB to prepare cross-sections for subsequent FIB and TEM investigations. TEM/EDX mapping revealed the qualitative elemental distribution over a certain area and TEM/EDX linescans provided quantitative information. In order to determine the crystal structure of the oxide, convergent beam electron diffraction (CBED) was used.



### *Steel Grain Boundary Regions*

A TEM cross-section bright field image, together with TEM/EDX elemental maps, of a steel grain boundary and the nearby base oxide after 24 h exposure are presented in Fig. 7a. Cr and Mn are depleted along the grain boundary, while Fe and Ni are enriched there. The Cr depleted part of the grain boundary is more than 2  $\mu\text{m}$  deep and stretches beyond the range of the map. However, the width of the depletion region is less than 200 nm. According to the linescans (Fig. 7b) along the line A–B indicated in Fig. 7a, the Cr concentration in the depletion region drops to below 10 wt.%, compared to 25 wt.% of the surrounding steel; at the grain boundary the Mn level is virtually zero; the Ni level goes up to  $\sim 35$  wt.% from  $\sim 20$  wt.%, while the Fe level increases only slightly.

### *Less-Oxidized Patches*

Less oxidized patches were found on almost all samples. A cross-section of a less oxidized patch beside an oxide nodule on the sample exposed for 168 h (Fig. 8a) shows two small steel grains lying underneath the patch. In most cases, the less oxidized patches are situated on top of small steel grains. The correlation of the less oxidized patches to small substrate grains has been reported for this alloy previously [21]. Sometimes “snowbanks” were observed surrounding the less oxidized patches. The small steel grains can vary in shape, but typically have a size of a few micrometers.

A STEM cross-section bright field image of a region containing a small steel grain is shown in Fig. 8b, together with the Cr and Ni EDX maps. The maps show that Cr is depleted, while Ni is enriched in the entire grain. Quantitative results show that the Cr concentration is low, around 10 wt.%, in the vicinity of the grain boundaries, and only slightly higher, 12 wt.%, in the center of the grain. The Fe and Ni levels are about 60 wt.% and about 30 wt.%, respectively in this grain.

### *Base Oxide*

*The Base Oxide on the 24-h Sample* Cross-section linescan data extending from the steel, across the steel–oxide interface and through the base oxide (indicated as the line CD in Fig. 7a) on the 24-h sample are presented in Fig. 9a. The base oxide is about 200 nm thick. The inner part of the base oxide is Cr-rich, around 80 wt.%, while the outer part is Cr poor, containing only 20 wt.% Cr and almost 80 wt.% Fe. The Mn level is relatively high (5 wt.%) in the Cr-rich inner layer. Si was observed at the oxide/steel interface and in the inner part of the base oxide. There is an around 100 nm deep Cr depleted zone (10 wt.% Cr) in the subjacent steel. The zone is enriched in Ni (40 wt.%).

*The Base Oxide on the 336-h Sample* The TEM/EDX linescan results (Fig. 9b) for the 336-h sample show the same trends as for the 24-h sample. However, the Cr concentration in the outer layer drops to  $\sim 15$  wt.% after 336 h, compared to

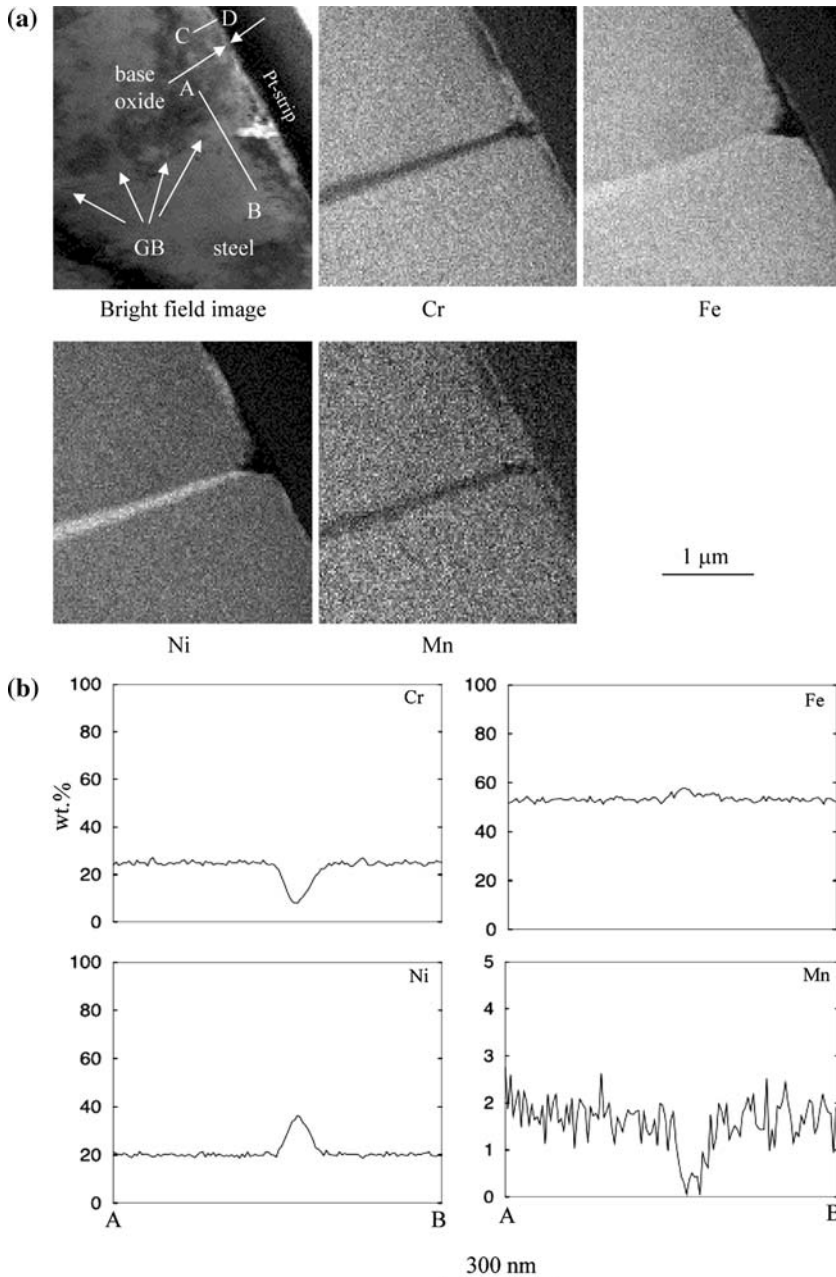


**Fig. 7** **a** STEM bright field image and EDX maps of a steel grain boundary (GB) and the base oxide scale on the 24-h sample. Cr and Mn are depleted along the GB, while Fe and Ni are enriched there. The GB depletion region is rather narrow (200 nm) and deep (more than 2 μm). The line AB, and CD indicate the position of the linescans shown in Figs. 7b and 9a, respectively. **b**. STEM/EDX linescan across the steel grain boundary indicated by AB in Fig. 7a. At the steel grain boundary the Cr concentration decreases from 25 wt.%, to around 10 wt.%, while the Ni concentration goes up to around 40 wt.%

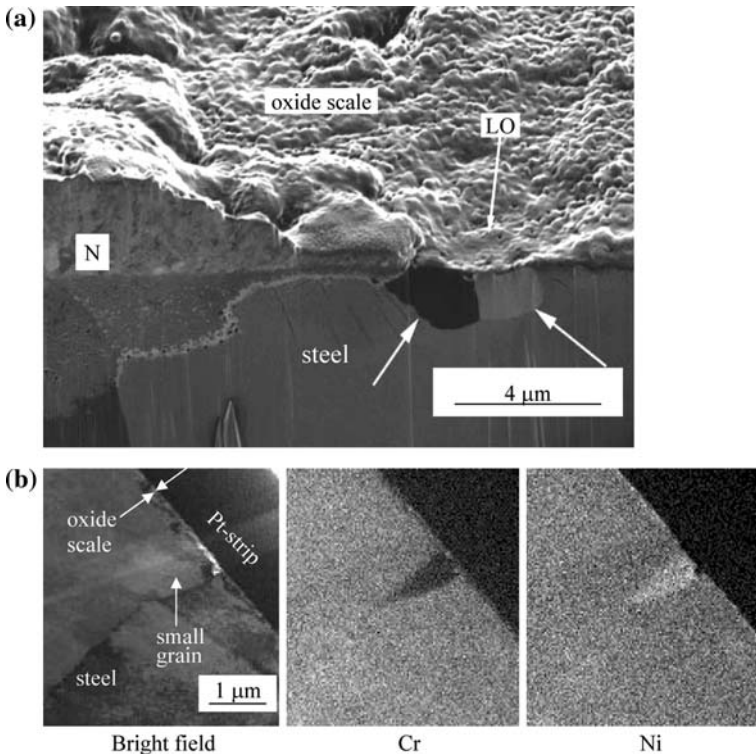


**Fig. 8** **a** FIB cross-section view of a less oxidized patch (LO) on the specimen exposed for 168 h (tilted 45°). Two small steel grains (*arrowed*) lie underneath the LO area. **b** STEM bright field image and EDX maps of a small steel grain in the 24-h sample. Cr is depleted, while Ni is enriched in the entire steel grain

~20 wt.% after 24 h. The base oxide evidently remains protective as long as the inner part of the scale is Cr-rich.

#### *Flat Oxide Nodules and “Snowbanks”*

Figure 10 shows a FIB cross-section view of a “snowbank” and several flat oxide nodules, on the 168-h sample. The crystallographic orientation contrast, resulting from different degrees of ion channeling for different crystal orientations, gives the location of the steel grain boundary, which is labeled as “GB” in the figure. FIB cross-section images with higher magnifications showed more clearly that both flat oxide nodules and “snowbanks” consist of two parts: the part above the original metal surface, which is referred to as the oxide “island”, and the part below, which is referred to as the oxide “crater”.

The cross-section of a thin, flat oxide nodule on the 24-h sample is shown in the TEM bright field image in Fig. 11a, accompanied by TEM/EDX element maps. Cr is enriched in the oxide crater. A continuous Cr depletion zone is present below the oxide scale, with a corresponding Ni enrichment. The oxide island and parts of the oxide crater are enriched in Fe. The distribution of Mn follows more or less that of Cr.

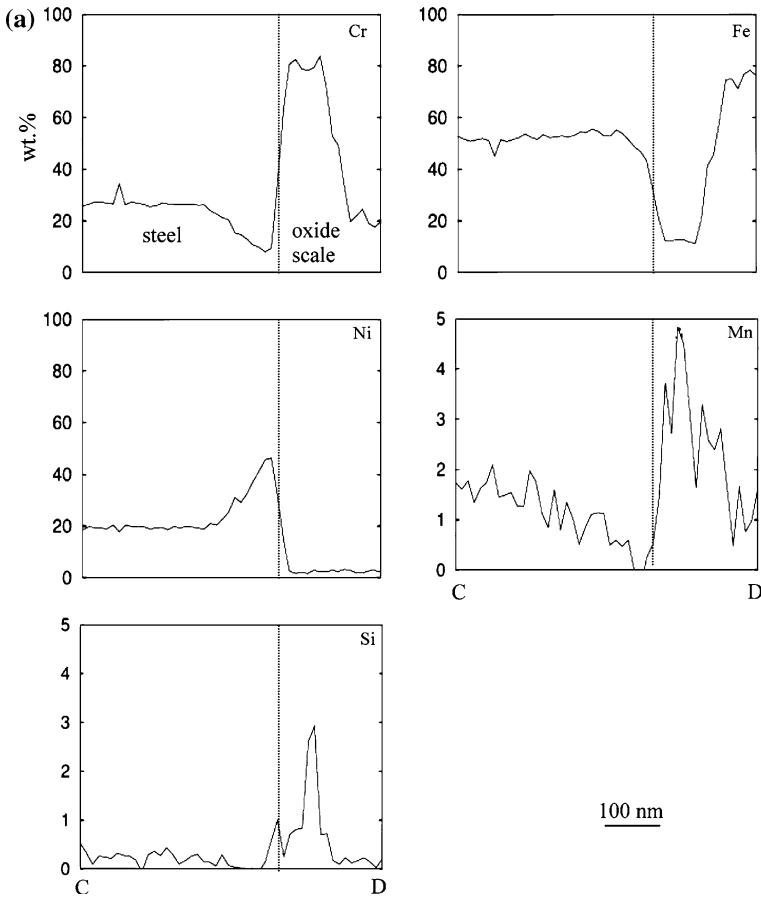


**Fig. 9** **a** STEM/EDX line scans across the steel and the base oxide layer (indicated by CD in Fig. 7a) on the 24-h sample. Cr is depleted and Ni is enriched in the steel below the oxide scale. The Cr concentration in the outer part of the base oxide is low. **b** STEM/EDX line scans across the steel and the base oxide on the 336-h sample. These results are rather similar to the results, shown in Fig. 9a, for the 24-h sample

Figure 11b shows line scan results (line AB in Fig. 11a) from the flat oxide nodule cross-section. The Cr level is 10 wt.% in the depletion zone, while Ni is enriched to 45 wt.% there. In the inner part of the crater, the Cr concentration reaches 80 wt.%, and in the outer part its concentration varies from 50 wt.% to 80 wt.%, whereas the Fe concentration varies from 30 wt.% to 15 wt.%. Two Ni peaks, 15 wt.% and 30 wt.%, were detected in the oxide island and the crater, respectively. The Mn concentration in the crater (3–5 wt.%) is higher than in the island. Si peaks (1 wt.%) were found at the metal/oxide interface and at the oxide crater/island interface.

A TEM bright field image, together with element maps, of a “snowbank” on the 336-h sample is displayed in Fig. 12a. Like the element distribution in the flat oxide nodule (Fig. 11a), Cr is enriched in the crater and relatively poor in the island, while

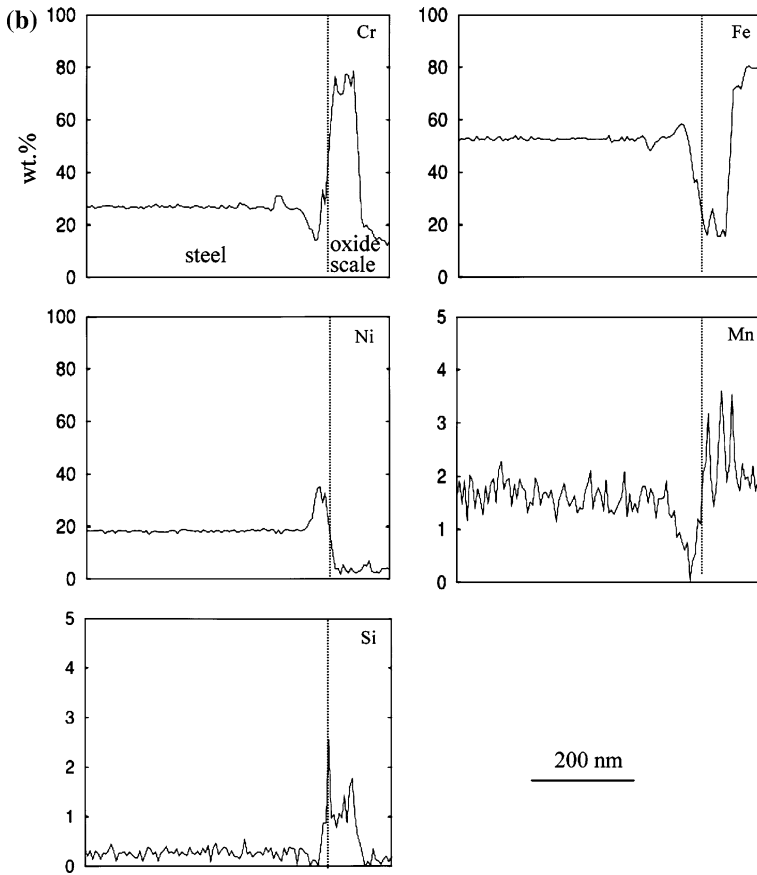


**Fig. 9** continued

Fe is poor in the crater and enriched in the island. Ni is enriched in the metal just below the crater; it is also present in the inner part of the island and in small amounts in the crater. In order to obtain quantitative information about the “snowbank”, cross-section linescans extending from the underlying steel through the “snowbank” (indicated as AB in Fig. 12a) were acquired. The results are shown in Fig. 12b. The Cr-rich oxide crater contains about 65–80 wt.% Cr, while the Fe-rich oxide island contains about 60–80 wt.% Fe. The inner part of the oxide island has a lower Fe concentration and corresponds to a region where the Ni level is higher, around 20 wt.%.

### *Large Oxide Nodules*

As noted in section “Evolution of the Oxide Features”, besides the base oxide scale and the submicron features, e.g. less oxidized patches, flat oxide nodules and

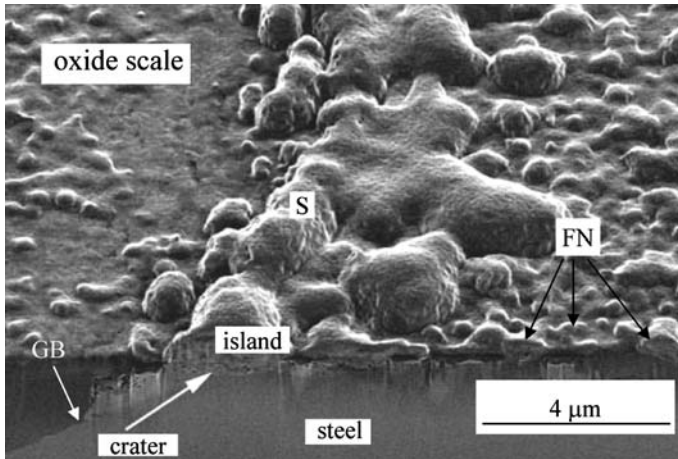


**Fig. 10** FIB cross-section view showing flat oxide nodules (FN) and a “snowbank” (S) beside a steel grain boundary (GB) on the 168-h sample (tilted 45°). Part of the oxide scale grew outwards (the oxide “island”) and part of it grew inwards (the oxide “crater”)

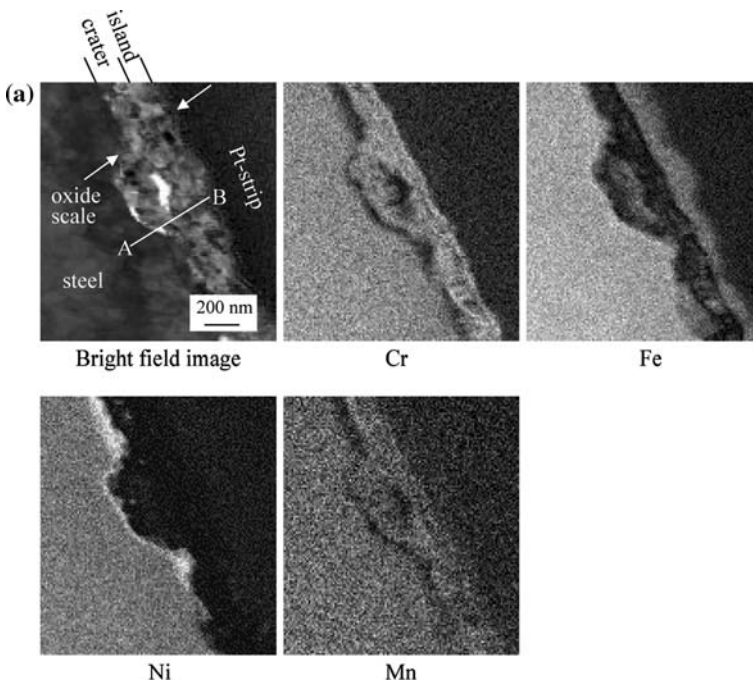


**Fig. 11 a** STEM bright field image and STEM/EDX maps of a flat oxide nodule on the 24-h sample. Cr is enriched in the oxide crater and deficient in the oxide island. A continuous Cr depletion/Ni enrichment zone lies underneath the oxide scale. The line AB, indicates the position of the linescans shown in Fig. 11b. **b** STEM/EDX linescans across a flat oxide nodule on the 24-h sample. In the inner part of the oxide crater, the Cr concentration is around 80 wt.%. Three Ni peaks are detected: in the metal, the oxide crater and the island, respectively

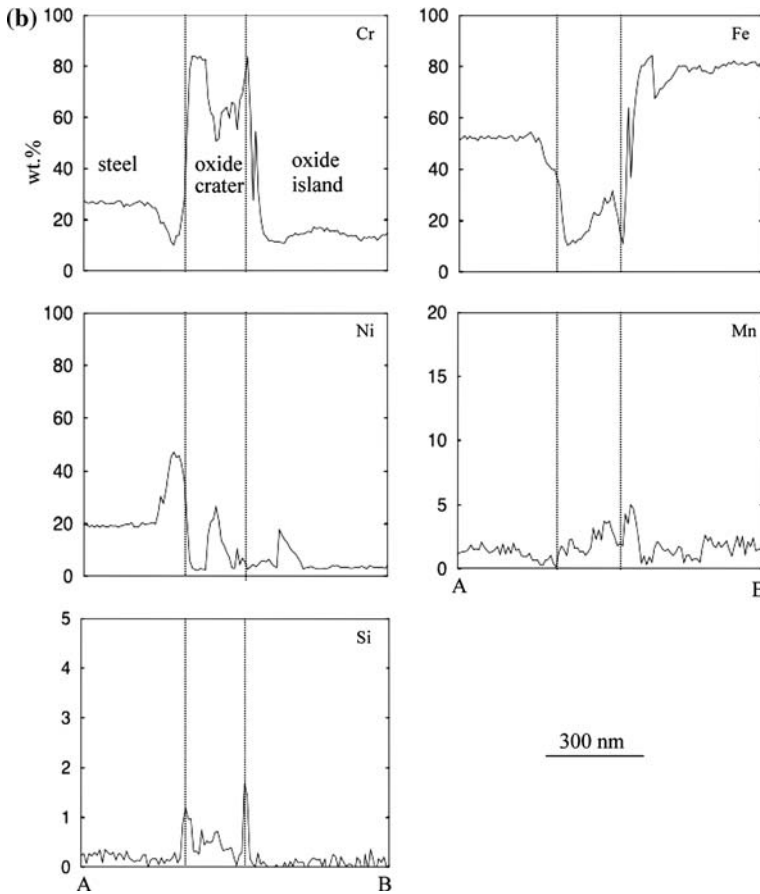


**Fig. 11** continued

“snowbanks”, large oxide nodules exist on some parts of the sample surface. This sub-section is dedicated to the study of these large nodules.

Cross-section views of two large oxide nodules on the 168-h sample are displayed in Fig. 13. The nodules, more than 10  $\mu\text{m}$  in width and 5  $\mu\text{m}$  in height, consist of an outward-growing oxide island and an inward-growing oxide crater. The depth of the crater is generally about the same as the height of the corresponding island.

Voids, porosities and cracks are often observed in the oxide nodules, both in the island and in the crater. The nodules grow laterally and eventually merge into a continuous layer. In this process, pores tend to form where the individual nodules come into contact. This is illustrated in Fig. 13a, where a region with porosity between two neighboring oxide islands is arrowed. In Fig. 13b voids and pores (arrowed) can be found between the oxide crater and the steel and within the oxide island.

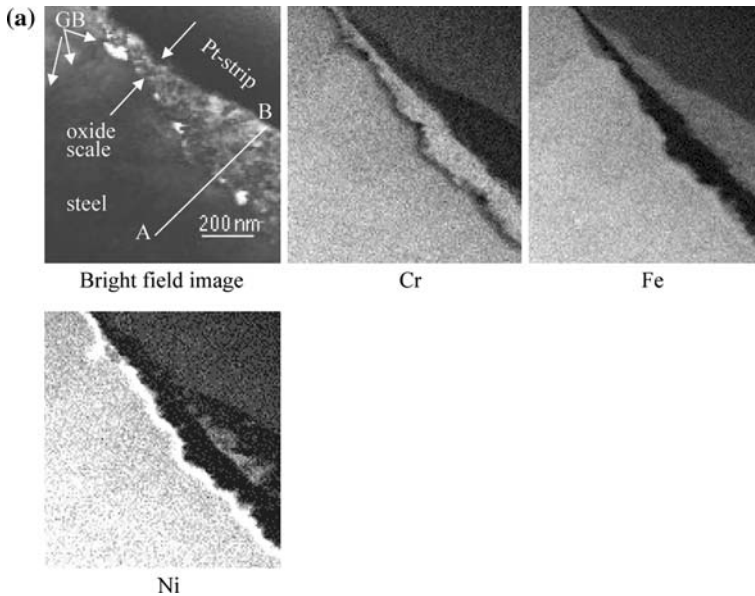


**Fig. 12 a** STEM bright field image and STEM/EDX maps of a “snowbank” on the 336-h sample. A linescan was performed along AB and the results are presented in Fig. 12b. The steel grain boundary is labeled GB. Cr is enriched in the oxide crater and deficient in the oxide island. A continuous Cr depleted zone is present below the oxide crater. Fe is deficient in the oxide crater and enriched in the oxide island. Ni is enriched in the continuous Cr-depleted zone and also in the inner part of the oxide island. **b** STEM/EDX linescans, across the steel and the “snowbank” (along AB in Fig. 12a). The Cr level is about 80 wt.% in the crater and 15 wt.% in the island, while the Fe level is approximately the opposite. The Ni level in the Ni-rich inner part of the island is about 15 wt.%

In order to analyze the nodules in more detail, the TEM was used. The bright field image and TEM/EDX maps in Fig. 14 show the distribution of elements in a large oxide nodule (around 15  $\mu\text{m}$  in size) formed on the 336-h sample. In the oxide island there are three porous regions, which appear bright in the bright field image and dark in all the elemental maps. The oxygen map shows the shape and the position of the oxide crater and island. The oxide crater contains more Cr and less Fe than the oxide island. The oxide island comprises two regions: a Ni-rich inner part and a Ni-poor, Fe-rich outer part. Ni is also present in the oxide crater, distributed inhomogeneously: some areas beneath the island’s Ni-rich regions have a relatively low Ni concentration, while some others, such as those close to the metal/crater interface, have a relatively high concentration. There is a Ni enriched zone along the island/crater interface except below the Ni-rich inner part of the island.

Since the elemental distribution varies much from place to place in the large oxide nodule, linescans for four representative regions were acquired:

- across the metal into the oxide crater (indicated as line AB in Fig. 14)
- across the oxide crater through the Ni-poor region of the oxide island (indicated as line CD in Fig. 14)



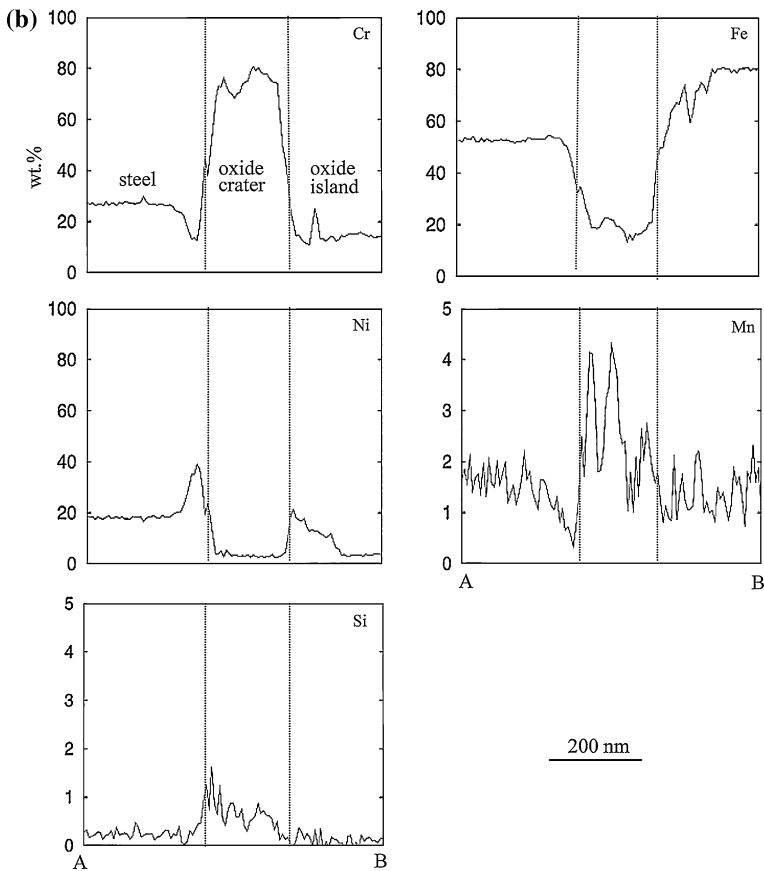


**Fig. 12** continued

- across the oxide crater through the Ni-rich region of the oxide island (indicated as line EF in Fig. 14)
- through the entire oxide island (indicated as line GH in Fig. 14)

The results are presented in the following sections.

*Linescan Across the Metal and the Oxide Crater* In Fig. 15 the cross-section EDX linescan data acquired across the steel/oxide crater interface are shown (line AB in Fig. 14). A slightly Cr-depleted ( $\sim 20$  wt.%), heavily Fe-depleted ( $< 20$  wt.%), and Ni-enriched (60 wt.%) zone was found in the steel adjacent to the oxide crater. Compared to the region underneath the base oxide, this zone is relatively less Cr-depleted and much more Fe-depleted. This indicates the large Fe consumption due to the nodule formation. In the oxide crater the Cr concentration varies from around 25 to 65 wt.%. The Fe level varies within a much narrower range (20–35 wt.%), while the Ni concentration varies from virtually 0 to 55 wt.%. Mn and Si are found in higher concentrations in the oxide crater than in the metal. Interestingly, the Ni

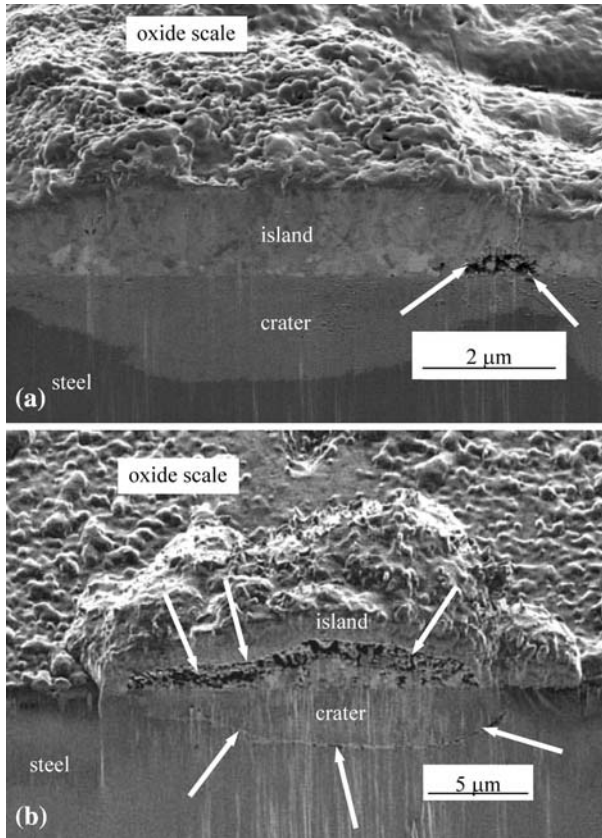


**Fig. 13** FIB cross section views of large oxide nodules on the 168-h sample (tilted 45°). The large nodules consist of an oxide “island” and an oxide “crater”. **a** Voids (arrowed) formed in the oxide island at the position where the two large oxide nodules have combined. **b** Considerable porosity within the oxide “island”, and also some voids at the steel/oxide scale interface can be seen

and the Cr profiles are more or less complementary, while the Fe and the Cr profiles show similar trends.

The above observation indicates the presence of two different compounds/phases: one enriched in mainly Fe and Cr and the other in Ni. A TEM bright field image from the oxide crater area is shown in Fig. 16a. The dark areas are Ni-rich and the bright areas contain virtually no Ni. The CBED pattern in Fig. 16b was acquired from a dark Ni-rich grain with a composition of 70 wt.% Ni, 10 wt.% Cr, and 15 wt.% Fe. The diffraction pattern could be indexed as a  $[1\bar{1}\bar{2}]$  fcc Ni-rich metal. The surrounding Ni-poor regions usually have a typical composition of 50 wt.% Cr, 5 wt.% Ni, 40 wt.% Fe. The diffraction pattern in Fig. 16c was taken from such an area. The pattern is indexed as  $[1\bar{1}\bar{2}]$  zone for  $(\text{Fe,Cr})_3\text{O}_4$  spinel. Thus in this region the crater contains a mixture of  $(\text{Fe,Cr})_3\text{O}_4$  and Ni-rich metal.

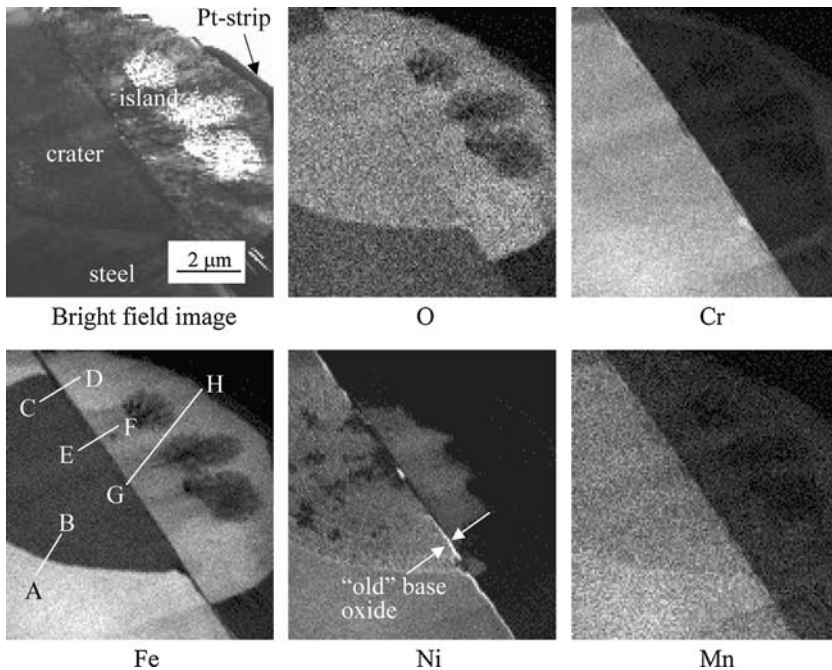


**Fig. 14** STEM bright field image and STEM/EDX maps of a large oxide nodule formed on the 336-h sample. Three large clusters of voids in the oxide island can be seen. Fe is enriched in the oxide island and deficient in the oxide crater. Ni is present in the inner part of the oxide island and in most part of the oxide crater. The position of four linescans are shown in the Fe map

*Linescan Across the Oxide Crater and the Oxide Island* Linescans perpendicular to the oxide crater/island interface and across the oxide crater through either the Ni-poor or the Ni-rich regions of the oxide island were acquired. The elemental distribution along a line from the oxide crater to the Ni-poor region (line CD in Fig. 14) in the island is shown in Fig. 17a. In the crater, the Cr concentration varies approximately between 25 and 70 wt.%. The Ni concentration varies from 5 to 55 wt.% in the crater, while it drops to almost zero in this part of the island. The Mn level is higher in the crater (2–4 wt.%) than in the island (<1 wt.%). Fe is the dominant element in the oxide island, with a concentration of around 90 wt.%.

Cross-section linescan results from the oxide crater to the Ni-rich region (line EF in Fig. 14) of the island are presented in Fig. 17b. In the crater the Cr concentration varies within narrow limits from 50 to 60 wt.%, indicating the presence of  $(\text{Fe,Cr})_3\text{O}_4$  spinel. The Cr concentration in the island is  $\sim 10$  t.%. The Fe and the Ni concentrations are rather constant, and are  $\sim 30$  and  $\sim 10$  wt.%, respectively in the crater, and  $\sim 60$  and  $\sim 30$  wt.%, respectively in the island. This suggests that Ni from this region of the crater has been transported outwards to the island to form the Ni-rich phase.

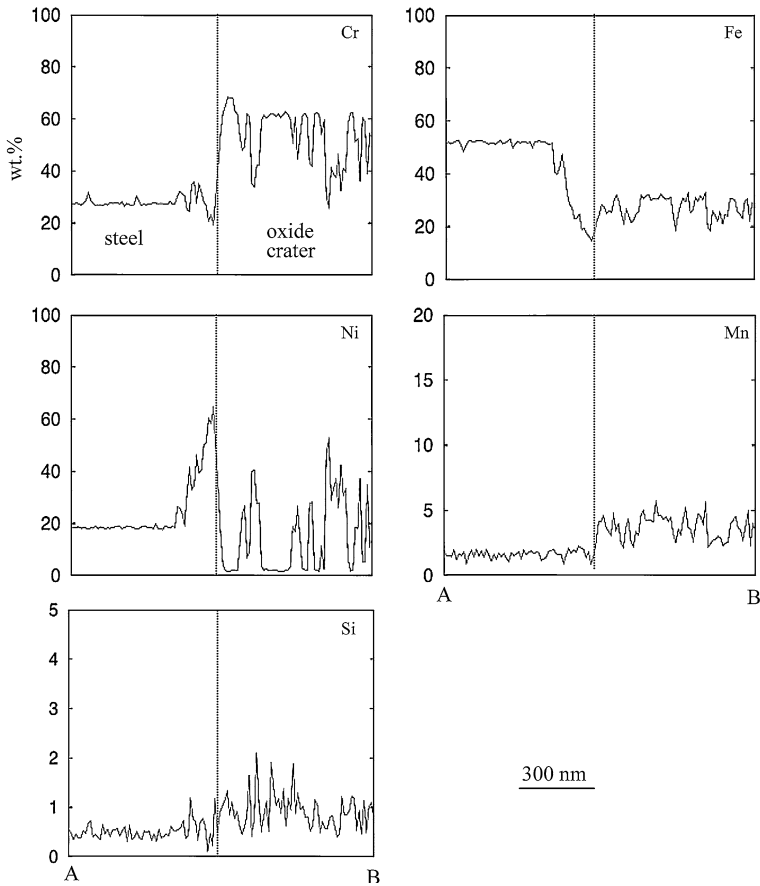


**Fig. 15** STEM/EDX linescans across the metal and the oxide crater (AB in Fig. 14) on the 336-h sample. In the oxide crater the Cr concentration varies from around 25 to 60 wt.%, and the Ni concentration varies from 5 to 55 wt.%, while the Fe level varies within a relatively narrow range (20–35 wt.%)

*Linescan Through the Entire Oxide Island* The island has a Ni-rich inner part and an Fe-rich outer part. The linescan results through the entire cross-section of the island (line GH in Fig. 14) are presented in Fig. 18. The Ni concentration is around 30 wt.% in the center, and drops to about 25 wt.% towards the edge of the inner part. The outer part contains virtually no Ni, slightly less than 10 wt.% Cr, and about 90 wt.% Fe.

Two electron diffraction patterns, acquired from the Ni-rich inner region and the Ni-free outer region, respectively, are shown in Fig. 19. The diffraction pattern from the inner region (Cr 10 wt.%, Ni 30 wt.%, Fe 60 wt.%) can be indexed as a  $[\bar{1}12]$  zone  $\text{Ni}(\text{Fe,Cr})_2\text{O}_4$  spinel. The outer Ni-free oxide (Cr 10 wt.%, Fe 90 wt.%) was indexed as  $[\bar{2}20\bar{1}]$  zone  $(\text{Fe,Cr})_2\text{O}_3$  corundum type oxide.

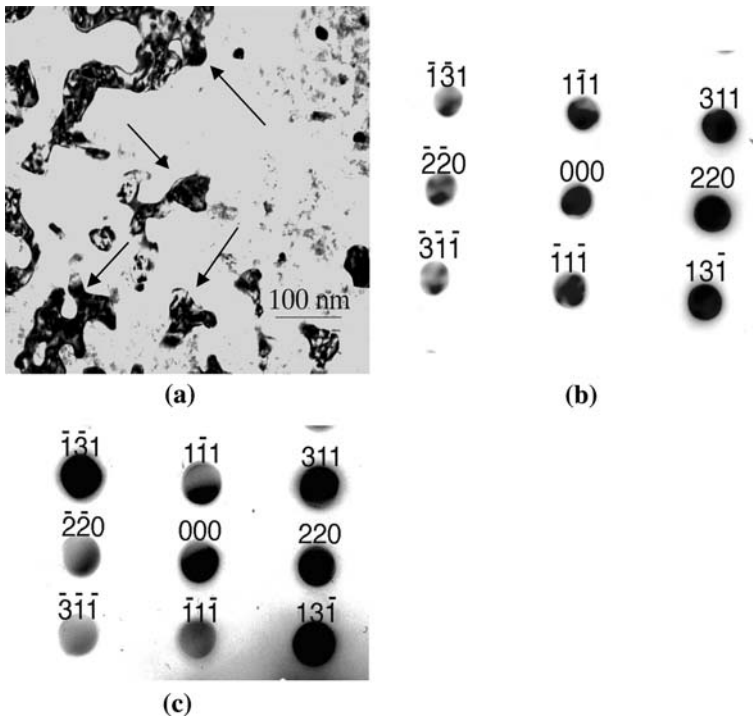


**Fig. 16** **a** TEM bright field image from the oxide crater showing the Ni-rich dark grains (*arrowed*) embedded in a bright Fe–Cr-rich region. **b** TEM diffraction pattern from the Ni-rich grain could be indexed as fcc Ni-rich metal. The zone axis is  $[1\bar{1}\bar{2}]$ . **c** TEM diffraction pattern from the surrounding Fe–Cr rich region, which could be indexed as a  $(\text{Fe,Cr})_3\text{O}_4$  spinel phase. The zone axis is  $[11\bar{2}]$

## Discussion

To summarize the observations and propose a model for the oxidation of 310 steel in  $\text{O}_2 + \text{H}_2\text{O}$  environment at  $600^\circ\text{C}$ , the evolution of the oxide scale is shown schematically in Fig. 20. Initially, a thin and protective base oxide, consisting of chromium-rich  $(\text{Fe,Cr})_2\text{O}_3$ , covers the whole sample surface. However, the base oxide exhibits variations in chromium content that are related to the steel microstructure and that determine its protective properties. Hence, some parts of the base oxide are poorer in chromium because the supply of chromium to the oxide is locally relatively slow. This typically affects parts of the surface that are far away from the steel grain boundaries which provide easy transport paths for chromium in the alloy. In the areas where the chromium content in the oxide is low, the protective  $(\text{Fe,Cr})_2\text{O}_3$  tends to be replaced by a rapidly growing duplex oxide consisting of inward-growing spinel (mainly  $(\text{Fe,Cr})_3\text{O}_4$ ) and an outward growing part consisting of relatively pure hematite ( $\text{Fe}_2\text{O}_3$ ). This behaviour is well-known for austenitic chromia forming steels, for example for alloy 304 in dry  $\text{O}_2$  or dry air at  $\geq 600^\circ\text{C}$  [12, 22]. The chromium content in  $(\text{Fe,Cr})_2\text{O}_3$  can vary from 0 to 100% and the

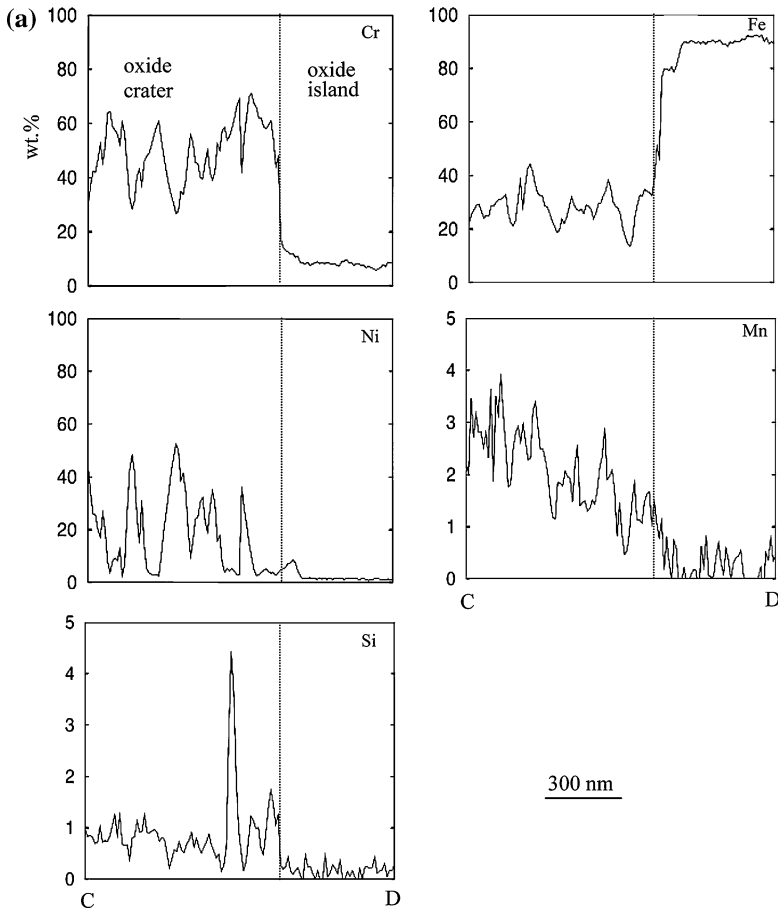


**Fig. 17** **a** STEM/EDX line scans through the oxide crater (CD in Fig. 14) to the Ni-free region of the island on the 336-h sample. In this part of the oxide island, the Fe concentration is around 90 wt.%, and the Cr concentration 10 wt.%. **b** STEM/EDX line scans through the oxide crater and the Ni-rich region of the island (EF in Fig. 14) on the 336-h sample. In this part of the oxide island the Ni level is around 33 wt.%

“chromia” formed on stainless steel always contains considerable amounts of iron in solid solution [20]. A comparison with our previous study [12] shows that the combination of water vapour and oxygen is far more corrosive towards alloy 304 than is dry  $O_2$  at this temperature. As discussed in the introduction, this effect is attributed to the vaporization of chromium from the oxide in the form of  $CrO_2(OH)_2(g)$  (see reaction 1). Hence, the tendency for local breakdown of the protective oxide in the present study is attributed mainly to chromium vaporization.

The present paper provides new information on the conversion of the protective oxide to a rapidly growing duplex scale and its time-dependence. The results illustrate the evolution of the scale subsequent to the breakdown of the original protective oxide. In some cases, a new “healing layer” consisting of Cr rich  $(Fe,Cr)_2O_3$  is formed at the bottom of the duplex scale. This results in the flat oxide

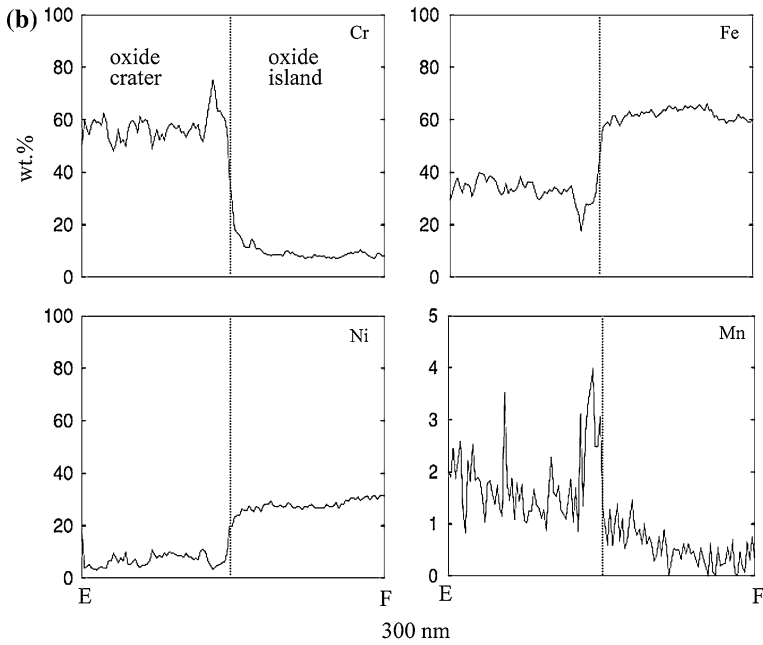


**Fig. 17** continued

nodules and in “snowbanks”. In other cases, the duplex oxide continues to grow rapidly throughout the exposure, resulting in the “large oxide nodules” (see Figs. 4, 5 and 6).

### Formation of the Base Oxide

The initial, protective, base oxide is illustrated in the TEM/EDX image in Fig. 7a (24 h), corresponding to step 1 in Fig. 20. The base oxide consists of a Cr-rich inner part and a Fe-rich outer part, with typical cationic concentrations of 80 wt.% Cr, and 80 wt.% Fe, respectively (Fig. 9a, b). The metal underneath is depleted in Cr. In a previous paper on the oxidation of alloy 310, it was reported that the evaporation of  $\text{CrO}_2(\text{OH})_2$  resulted in a lower Cr/Fe ratio in the oxide formed in the presence of  $\text{O}_2 + \text{H}_2\text{O}$  (See Eq. 1) compared to samples exposed to dry  $\text{O}_2$  [21]. Hence, the rather low Cr content observed in the outer part of the scale in this case is partly attributed to  $\text{CrO}_2(\text{OH})_2$  evaporation. The Cr-depleted zone in the metal is due to rapid Cr consumption by the formation of the Cr-rich oxide in combination with a relatively slow Cr supply from the subjacent steel region.

An inspection of the corresponding plan view image in Fig. 1b shows a lateral variation in the appearance of the oxidized surface, appearing as a network of lines that corresponds with the grain structure of the metal substrate. This variation is further illustrated by the FIB image of the same sample in Fig. 3, showing that the oxide formed over the metal grain boundaries is smoother than the oxide formed above the centre of the grains (Fig. 3 also shows oxide nodules (N) which are not

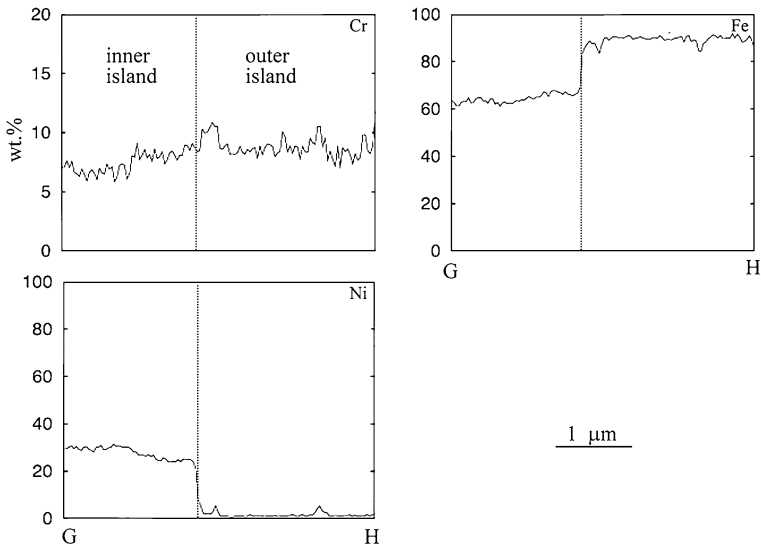


**Fig. 18** STEM/EDX linescans acquired vertically across the oxide island (GH in Fig. 14) on the 336-h sample. Across the Ni-rich/Ni-free region interface, the Ni concentration decreases from 30 wt.% to almost zero. The Cr level is about the same in both regions, about 10 wt.%

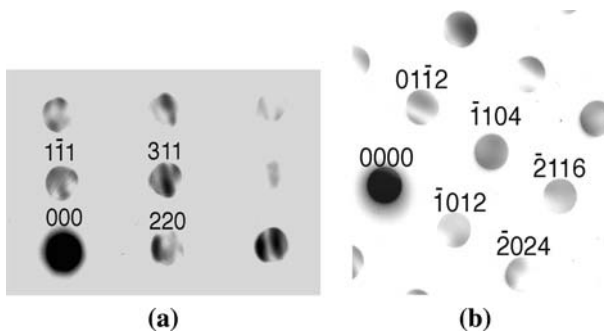


**Fig. 19** **a** CBED pattern from the Ni-rich inner region, which has been indexed as  $(\text{Fe,Cr})_2\text{NiO}_4$  spinel phase. The zone axis  $[\bar{1}12]$ . **b** CBED pattern from the Ni-free outer shell, which could be indexed as  $(\text{Fe,Cr})_2\text{O}_3$  corundum phase. The zone axis  $[\bar{2}20\bar{1}]$

considered in this case). It is well known that the grain boundaries provide easy diffusion paths for Cr in austenitic stainless steels, allowing for a faster Cr supply in these regions compared to at the center of the steel grains. Hence, it is suggested that the difference in oxide morphology is due to differences in the supply of Cr to the oxide by diffusion in the alloy [23–25]. The variation in the width of the smooth grain boundary regions in the base oxide (Fig. 3) is suggested to be due to variations in the rates of Cr supply for different grain boundaries. It may be noted that, for small steel grains, the entire grain can act as a grain boundary region providing better protection, leading to the formation of less oxidized patches. Other authors also reported better protection of small steel grains [24, 26].



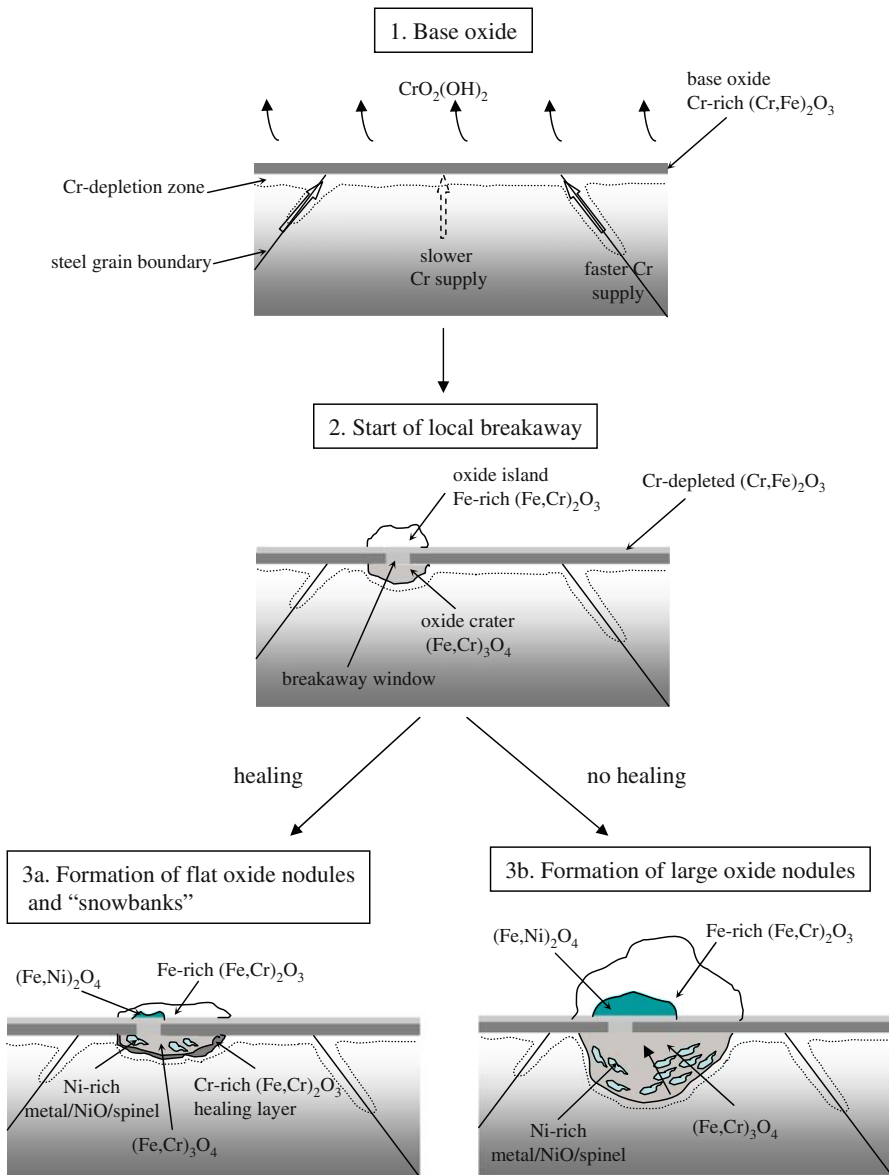


**Fig. 20** Schematic drawing of the evolution of the oxide scale formed on 310 stainless steel at  $600\text{ }^{\circ}\text{C}$  in the presence of  $\text{O}_2 + 40\% \text{H}_2\text{O}$

### Start of Breakaway Oxidation

As the Cr concentration in the oxide scale drops below a certain critical level (locally) due to Cr loss through water vapour induced Cr evaporation, the scale loses its protectiveness, and local breakaway oxidation commences (shown Fig. 20 step

2). Figures 3, 4, 5 and 6 show different oxide features due to local breakaway: i.e. large oxide nodules, thin flat oxide nodules and snowbanks. The FIB and TEM cross-section analyses (Fig. 8a, 10, 11a, 12a, 13, 14) show that when the “old” base oxide loses its protectiveness locally, anion and cation transport through this “window” in the base oxide becomes fast. As a result, an outward growing oxide island (relatively pure  $\text{Fe}_2\text{O}_3$ ) and an inward growing oxide crater (mainly  $(\text{Fe,Cr})_3\text{O}_4$ ) form. With time Ni is incorporated into the oxide crater in the form of Ni-rich metal particles as detected in the present study and/or NiO and/or  $(\text{Fe,Ni})_3\text{O}_4$  as reported earlier [27]. The presence of Ni(s) in the bottom part of the scale is suggested to be a consequence of the gradual enrichment of Ni in the remaining alloy by oxidation. At low oxygen potential, this process will eventually lead to the formation of a mixture of iron and chromium oxides and metallic Ni. As oxidation proceeds, the metallic Ni particles will experience increasingly oxidizing conditions and will convert to oxide. It is expected that Ni will then gradually diffuse into the Fe-rich oxide island to form Fe–Ni spinel.

#### Formation of Flat Oxide Nodules/“Snowbanks”

Following the breakaway oxidation flat oxide nodules/“snowbanks” sometimes form (Fig. 20 step 3a). At the bottom of the oxide crater there is a layer with about 80 wt.% (corresponding  $\sim 80$  at.%) Cr in both the flat oxide nodules and “snowbanks” (Figs. 11b, 12b). The maximum cation concentration of Cr in  $(\text{Fe,Cr})_3\text{O}_4$  spinel is 67 at.%, implying that the bottom part of the flat oxide nodules and “snowbanks” contain a protective Cr-rich  $(\text{Fe,Cr})_2\text{O}_3$  phase. In a previous study [21] it was reported that a Cr-rich corundum type oxide had formed at the bottom of the oxide crater.

A probable explanation for the above observations is proposed to be local transient breakaway oxidation followed by re-formation of a Cr-rich  $\text{M}_2\text{O}_3$  corundum phase. The outward growing Fe-rich island, formed as a result of local breakaway, is expected to decrease Cr evaporation [27]. In addition, the rapid consumption of Fe and Ni results in a recovery of the Cr level in the steel just below the metal/oxide crater interface. It is suggested that these effects cause the Cr content in the alloy to become sufficiently high in order for a new layer of Cr-rich  $(\text{Fe,Cr})_2\text{O}_3$  to form (see Evans et al. [28]). In this way nodule growth is suppressed, resulting in the “flat nodules and “snowbank” features.

Flat oxide nodules and “snowbanks” are present on the samples exposed for more than 24 h. The formation mechanism is believed to be the same for both features, i.e. “snowbanks” correspond to flat oxide nodules formed close to and along the steel grain boundaries. The prevalence of “snowbanks” close to steel grain boundaries could be because steel regions neighboring the steel grain boundaries tend to be depleted in Cr. Thus a local breakaway can be triggered more easily there, followed by re-healing.

#### Formation of Large Oxide Nodules

If re-formation of a Cr-rich corundum-type oxide layer at the bottom of the oxide crater fails, rapid oxidation continues via the non-protective “window” in the base

oxide and large oxide nodules form (Fig. 20, step 3b). Compared to the size of the large oxide nodules, the “window” is rather small. This observation is consistent with the previous study on the microstructure of the oxide scale formed on 304L, where only a central spot of 1–2  $\mu\text{m}$  diameter in the “old” base oxide below the 10  $\mu\text{m}$  island was found to be non-protective [27]. The transport of cations, including Ni, through this non-protective “window” results in a “radial” pattern microstructure in the oxide island.  $\text{Ni}(\text{Fe},\text{Cr})_2\text{O}_4$  spinel is present in the center of the island, above the “window”. The crater microstructure also has a radial pattern. The Ni-rich regions become more frequent with increasing distance to the breakaway “window”. The crater consists of a semi-circular pattern of alternating Ni-poor ( $\text{Fe}(\text{Fe},\text{Cr})_2\text{O}_4$  spinel) and Ni-rich (metal or NiO and/or  $(\text{Fe},\text{Ni})_3\text{O}_4$ ) bands. The bands are parallel to the metal/oxide interface, i.e., perpendicular to the growth direction. It is suggested that the alternating nickel free and nickel rich bands form as the oxide crater grows inwards. The formation of Fe–Ni spinel in the oxide island consumes nickel from the crater, leading to the observed depletion of Ni just below the breakaway window.

Re-formation of Cr-rich oxide can also occur in the oxide craters of large nodules. In the present study, at some positions at the bottom of large oxide craters the Cr concentration reaches 80 wt.%, indicating the likely presence of a re-formed protective Cr-rich  $(\text{Fe},\text{Cr})_2\text{O}_3$  oxide. However, whether these chromia rich regions prevent further nodule growth is not clear from the present investigation.

#### Further Evolution of the Oxide Scale

No new oxide features were observed on the sample surfaces following 168 and 336-h exposures. The oxidation proceeds all over the surface, also in the grain boundary regions. As observed in this study, the steel grain boundary oxide “net” tends to become vaguer with time. One can expect that it will eventually vanish. Thick oxide covering the whole surface would be consistent with the observations by Evans of no special grain boundary effect on a 20 wt.% Cr/25 wt.% Ni stainless steel oxidized at 1123 K for 6000 h [29]. In addition, after 336 h exposure flat oxide nodules and “snowbanks” developed on almost all the steel grains. On the other hand, large nodules were only observed occasionally. This indicates that the re-healed oxide scale can remain protective for a long time.

#### Comparison with other Steels

The oxidation behavior of the two austenitic stainless steels, type 310 and type 304L show many similarities. However, in the case of 304L, there was little evidence for oxide features like “snowbanks”, flat oxide nodules, and Cr-rich healing layers (J. E. Tang et al. unpublished). This may be because that the Cr concentration in 304L is too low to allow the re-formation of a Cr-rich healing layer in the present exposure conditions. This indicates that there is an environment dependent, critical Cr concentration in austenitic steels for re-forming a Cr-rich healing oxide layer, as proposed by Evans et al. [28, 29]. Additionally, since type 304L stainless steel has a much lower Ni concentration than type 310, the oxide islands on 304L seldom exhibit  $(\text{Fe},\text{Cr})_2\text{NiO}_4$  spinel formation.

Compared to the austenite type 310 stainless steel, the ferritic/martensitic steel X20 has a lower Cr level ( $\sim 11$  wt.%). However, the rate of Cr diffusion in X20 is faster, because of the inherent properties of the metal as well as because of the smaller grain size. Under the same oxidation environment as that used in this study, X20 forms a protective thin Cr-rich  $(\text{Fe,Cr})_2\text{O}_3$  oxide scale over the entire sample surface. However, the scale remains protective only for a limited time (less than 168 h). After that, the entire sample suddenly suffers a breakaway oxidation [14, 15], forming a uniform double-layered thick oxide scale, corresponding to an island and crater formation on the whole sample [30]. No healing of the oxide was observed for X20.

## Conclusions

The present paper shows that the evolution of the oxide scale on 310 stainless steel at 600 °C in the presence of  $\text{O}_2 + 40\% \text{H}_2\text{O}$  depends on the competition between water vapor induced Cr loss from the oxide scale and replenishment of Cr from the substrate steel. A thin protective base oxide is formed after a short time. Because of faster Cr replenishment, the steel grain boundary regions are more protective than the steel grain centers. This explains why small steel grains provide better protection, forming less-oxidized patches. Cr evaporation triggers local breakdown of the protective oxide scale when the Cr concentration in the oxide drops below a critical level, resulting in the formation of oxide nodules. The evolution of the oxide nodules is determined by the ability to re-form a Cr-rich protective healing layer. If such a new protective layer is formed, the growth of the nodule ceases and flat oxide nodules or “snowbanks” result; if this does not happen, fast breakaway oxidation continues and large oxide nodules are formed. Although on a much smaller scale, the microstructure of flat oxide nodules and “snowbanks” is similar to that of large oxide nodules: the island part of the nodule contains an inner part of  $(\text{Fe,Ni})$  spinel and an outer part of Fe-rich (90 wt.%)  $(\text{Fe,Cr})_2\text{O}_3$ , and the crater contains Ni-poor  $(\text{Fe(Fe,Cr)}_2\text{O}_4)$  spinel and Ni-rich (metal and/or NiO and/or  $(\text{Fe,Ni})_3\text{O}_4$ ) regions. In the large nodules the distribution of different phases exhibits a pronounced “radial” pattern.

**Acknowledgements** This work was carried out within the Swedish High Temperature Corrosion centre (HTC) with financial support partly provided by the Swedish National Research Council (VR).

## References

1. W. H. Hatfield, in *Iron and Steel Institute—Meeting*, Vol. 9 (Iron and Steel Institute, 1927), p. 26.
2. C. T. Fujii and R. A. Meussner, *Journal of Electrochemical Society* **111**, 1215 (1964).
3. I. Kvernes, M. Oliveira, and P. Kofstad, *Corrosion Science* **17**, 237 (1977).
4. P. Kofstad, in *High Temperature Corrosion, Elsevier Applied Science*, Chapter 11 (1988), pp. 342–387.
5. D. Caplan and M. Cohen, *Journal of Electrochemical Society* **108**, 438 (1961).
6. D. Caplan and M. Cohen, *Corrosion* **15**, 141t (1959).
7. A. Rahmel and J. Tobolski, *Corrosion Science* **5**, 333 (1965).

8. M. Thiele, H. Teichmann, W. Schwarz, and W. J. Quadakkers, *VGB Kraftwerkstechnik* **2**, 129 (1997).
9. A. Holt and P. Kofstad, *Solid State Ionics* **69**, 137 (1994).
10. S. Jiannian, Z. Lingjiang, and L. Tiefan, *Oxidation of Metals* **48**, 347 (1997).
11. W. J. Quadakkers and P. J. Ennis, *VGB Kraftwerkstechnik* **2**, 123 (1997).
12. H. Asteman, J.-E. Svensson, L.-G. Johansson, and M. Norell, *Oxidation of Metals* **52**, 95 (1999).
13. H. Asteman, J.-E. Svensson, and L.-G. Johansson, *Oxidation of Metals* **57**, 193 (2002).
14. K. Segerdal, J.-E. Svensson, and L.-G. Johansson, *Materials and Corrosion* **53**, 247 (2002).
15. K. Segerdal, J.-E. Svensson, and L.-G. Johansson, *Materials and Corrosion* **53**, 479 (2002).
16. H. Asteman, K. Segerdal, J.-E. Svensson, and L.-G. Johansson, *Materials Science Forum* **369–372**, 277 (2001).
17. H. Asteman, J.-E. Svensson, and L.-G. Johansson, *Corrosion Science* **44**, 2635 (2002).
18. A. Yamauchi, K. Kurokawa, and H. Takahashi, *Oxidation of Metals* **59**, 517 (2003).
19. E. Opila, *Materials Science Forum* **461–464**, 765 (2004).
20. G. C. Wood and D. P. Whittle, *Corrosion Science* **7**, 763 (1967).
21. J. E. Tang, F. Liu, H. Asteman, J.-E. Svensson, L.-G. Johansson, and M. Halvarsson, *Materials at High Temperatures* **24**, 27 (2007).
22. I. Saeki, T. Saito, R. Furuichi, H. Konno, T. Nakamura, K. Mabuchi, and M. Itoh, *Corrosion Science* **40**, 1295 (1998).
23. X. Peng, J. Yan, Y. Zhou, and F. Wang, *Acta Materialia* **53**, 5079 (2005).
24. S. N. Basu and G. J. Yurek, *Oxidation of Metals* **36**, 281 (1991).
25. G. J. Yurek, D. Eisen, and A. Garratt-Reed, *Metallurgical and Materials Transactions A* **13**, 473 (1982).
26. D. R. Baer and M. D. Merz, *Metallurgical Transactions A* **11A**, 1973 (1980).
27. M. Halvarsson, J. E. Tang, H. Asteman, J.-E. Svensson, and L.-G. Johansson, *Corrosion Science* **48**, 2014 (2006).
28. H. E. Evans, A. T. Donaldson, and T. C. Gilmour, *Oxidation of Metals* **52**, 379 (1999).
29. H. E. Evans, D. A. Hilton, R. A. Holm, and S. J. Webster, *Oxidation of Metals* **14**, 235 (1980).
30. F. Liu, J. E. Tang, T. Jonsson, S. Cnovic, K. Segerdal, J.-E. Svensson, and M. Halvarsson, *Oxidation of Metals* **66**, 295 (2006).